Precisely computing phonons via irreducible derivatives

Sasaank Bandi● and C. A. Marianetti●

Department of Applied Physics and Applied Mathematics, Columbia University, New York, New York 10027, USA

Computing phonons from first principles is typically considered a solved problem, yet inadequacies in existing techniques continue to yield deficient results in systems with sensitive phonons. Here we circumvent this issue using the lone irreducible derivative (LID) and bundled irreducible derivative (BID) approaches to computing phonons via finite displacements, where the former optimizes precision via energy derivatives and the latter provides the most efficient algorithm using force derivatives. A condition number optimized basis for BID is derived which guarantees the minimum amplification of error. Additionally, a hybrid LID-BID approach is formulated, in which select irreducible derivatives computed using LID replace BID results. We illustrate our approach on two prototypical systems with sensitive phonons: the shape memory alloy AuZn and metallic lithium. Comparing our resulting phonons in the aforementioned crystals to calculations in the literature reveals nontrivial inaccuracies. Our approaches can be fully automated, making them well suited for both niche systems of interest and high-throughput approaches.

I. INTRODUCTION

The Born-Oppenheimer potential characterizes the total energy of a collection of nuclei and electrons at zero temperature, where the nuclei are localized at specific positions. The second-order Taylor series for some reference configuration provides a vibrational Hamiltonian for the nuclei, from which the phonons may be constructed. Given the importance of phonons for materials properties, precisely and efficiently computing the Taylor series of the Born-Oppenheimer potential from first principles is critical. While perturbative approaches to computing phonons have their merits, finite-displacement approaches are agnostic to the first-principles methodology and their implementations [1]. Therefore, the development of advanced finite-displacement methodologies which can knowingly balance precision and efficiency is paramount. Previously, we introduced approaches to compute phonons and their interactions via irreducible derivatives (IDs) [1], and here we focus exclusively on phonons and introduce several important technical developments.

Our irreducible approaches begin by building a vibrational Hamiltonian purely in terms of space group irreducible derivatives, such that all space group symmetry and the homogeneity of space (e.g., acoustic sum rules) are satisfied by construction. Each ID will then be associated with the smallest commensurate supercell allowed by group theory, which will require the use of nondiagonal supercells in general. At this stage, the IDs may be constructed via finite difference using either the second energy derivatives or the first force derivatives. The use of energy derivatives implies that each ID is measured independently, and the method which isolates IDs is referred to as the lone irreducible derivative (LID) approach. Alternatively, the use of force derivatives enables multiple IDs to be measured simultaneously, and when the IDs are computed in the fewest number of measurements and smallest supercells allowed by group theory, this is referred to as the hierarchical supercell bundled irreducible derivative (BID)

approach. BID may also be conducted in a single supercell commensurate with all q points, although this is normally not desirable given the scaling of typical first-principles approaches, and therefore, BID will always imply hierarchical supercell BID. The LID approach can also be applied to force derivatives, where one computes the smallest number of IDs as possible in a given measurement, and therefore, LID with forces can be viewed as a minimal bundling approach. We refer to LID with energy derivatives as LID_0 and that with force derivatives as LID_1. Given that energy derivatives normally converge faster than force derivatives with respect to the convergence parameters, LID_0 is normally more accurate than LID_1 and BID for a given set of convergence parameters. Moreover, LID_1 is normally more accurate than BID, given that bundling combines many irreducible representations. Of course, for a given set of convergence parameters, BID is substantially more efficient than LID_1, which is somewhat more efficient than LID_0. Therefore, it is always preferable to use BID, but care is needed to ensure that proper convergence is obtained. In this paper, we derive the best possible way to numerically execute BID and outline a method to selectively hybridize LID and BID if needed.

When performing a BID calculation, a measurement basis is required to perform finite-difference calculations, and there are an infinite number of choices. Previously, we introduced the notion of a condition number optimized (CNO) measurement basis [1], in which there is a minimum amplification of error between the measurements and the irreducible derivatives. However, we did not previously solve the problem of how to find the measurement basis, and in this work we present the solution for second order, demonstrating that zero amplification of error can be achieved. It should be noted that mainstream finite-displacement methods to compute phonons [2–4] are a type of single-supercell BID (see [1] for a detailed discussion). However, these approaches are not condition number optimized with respect to the irreducible derivatives,

which are the quantities that are most directly probed by experiment (e.g., inelastic neutron scattering).

Given some first-principles theory, different methods for computing phonons may yield different results due to sensitivity, and each method will have a different trade-off between efficiency and accuracy. In the context of density functional theory (DFT), density functional perturbation theory (DFPT) might be considered the definitive solution, but DFPT still must be converged with respect to various discretization parameters such as k points and the basis set cutoff, which may be nontrivial. While DFPT has been implemented using the tetrahedron method [5], where convergence with respect to k-point density has been extensively studied, nearly all existing studies used smearing integration methods, which are more difficult to properly extrapolate to zero discretization given that both k-point density and a smearing parameter must be varied. In any case, results from DFPT must be properly converged in order to obtain numerically exact solutions. Finite-displacement techniques utilize either the energy or the forces, which must be converged with respect to the same discretization parameters, but each observable converges at a different rate. An additional consideration for finite-displacement techniques is convergence with respect to the finite-displacement discretization Δ. If Δ is excessively small, impractical values of DFT convergence parameters will be needed, while if Δ is excessively large, anharmonic contributions will deviate from leading order. Therefore, it is imperative to execute multiple Δ and resolve the known leading-order behavior (e.g., quadratic for central finite difference), such that the derivative is precisely extrapolated to $\Delta = 0$; we refer to this process as the construction of quadratic error tails. The substantial gains in efficiency allowed by our irreducible derivative methods can be converted to gains in precision by properly converging finite-displacement calculations in all regards. Moreover, sensitivities are often associated with particular phonon modes (e.g., see Sec. III), and our approaches inherently isolate such sensitivities; however, conventional approaches inherently mix them, making the practical task of converging results much more challenging.

While the LID and BID methods were developed in the context of computing symmetrized displacement derivatives, they can be applied without modification to arbitrary-order strain derivatives, which we refer to as ϵ-LID and ϵ-BID (see Ref. [6] for up to fourth-order strain derivatives computed using ϵ-LID). Here we focus on only second strain derivatives (i.e., linear elastic constants). Given that the elastic constants dictate the linear phonon dispersion at small q, precisely computing the elastic constants is an integral component of precisely computing the phonons. When applying ϵ-LID and ϵ-BID, the strains are symmetrized according to irreducible representations of the point group, such that the usual group theoretical selection rules dictate the strain irreducible derivatives *a priori* (i.e., intrinsic symmetrization [1]). For ϵ-LID$_0$, the elastic constants are computed using second energy derivatives, while ϵ-LID$_1$ and ϵ-BID use first stress derivatives, and ϵ-BID measures all irreducible strain derivatives in the fewest measurements possible via bundling. As in the case of phonons, ϵ-LID$_0$ will normally be the most precise approach for a given set of convergence parameters as energy

derivatives are easier to converge than stress derivatives, but ϵ-BID will be the most efficient. Conventional approaches for performing high-throughput elastic constant calculations are perhaps best considered a type of ϵ-LID$_1$ [7], which is a reasonable philosophy for high-throughput calculations, but ϵ-LID$_0$ should be used when a definitive answer is needed. In this study, all elastic constants are computed using ϵ-LID$_0$.

To illustrate our methodological developments, we perform calculations on the shape memory alloy AuZn and bcc Li. We study AuZn in both the cubic structure (space group 221) and the low-symmetry trigonal phase (space group 143) [8], which is formed in a martensitic transition at $T = 64$ K [9]. The phonons have been extensively explored in the cubic phase using DFT [10], although the results had numerous sensitivities based on the details of the computational approach. We also study the phonons of Li, which have been measured using inelastic neutron scattering [11]. Recent DFT calculations exhibit anomalous features in the phonon dispersion which are not present in experiment [12], and we will demonstrate that the most substantial anomaly is due to a lack of numerical precision.

II. BID AND THE CNO MEASUREMENT BASIS

We begin by providing the formulation of BID at second order. Consider a real function $V(u_1, \ldots, u_N)$ invariant to some group, where all independent second derivatives must be extracted. Assume that evaluating V at some arbitrary $\{u_1, \ldots, u_N\}$ has a nontrivial computational cost but also provides all first derivatives $\{\frac{\partial V}{\partial u_i}\}$, also denoted $\{F_i\}$, subject to random noise. First-order finite-difference calculations may then be used to construct second derivatives, which contain random noise from the first derivatives. A "measurement vector" is defined as a vector in the N-dimensional space of displacements. BID is the method which computes all N_d independent second derivatives in the smallest number of measurements N_m. In the absence of symmetry, we have $N_d = N(N + 1)/2$, but this number will be reduced when the group contains operations other than the identity. A measurement along the measurement vector θ_i will yield N second derivatives which are then stacked into a vector $\boldsymbol{f}_i = (\frac{\partial F_1}{\partial \theta_i}, \ldots, \frac{\partial F_N}{\partial \theta_i})^{\mathsf{T}}$. A given $\boldsymbol{f}_i$ can then be related to the vector of irreducible derivatives it probes, denoted $\boldsymbol{d}_i$, via the "chain rule matrix" $\boldsymbol{C}_i$ as $\boldsymbol{f}_i = \boldsymbol{C}_i \boldsymbol{d}_i$. The smallest number of measurements which probe all irreducible derivatives is then chosen, yielding N_m. There will be an infinite number of sets of measurement vectors, and some criteria must be employed to select an optimum choice.

Previously, we introduced the notion of a CNO measurement basis [1], and in the present formulation the measurement vectors $\{\theta_1, \ldots, \theta_{N_m}\}$ are condition number optimized if the condition number of all $\boldsymbol{C}_i$ is 1. The condition number of a matrix can be computed as the ratio of the largest and smallest singular values and is a measure of the maximum error amplification when solving a linear system of equations. The BID method at second order and the CNO measurement basis are now formally defined, but we are still left with the problem of how to determine the CNO basis.

In order to determine N_m and the CNO basis, we first restrict ourselves to the case of an ambivalent group, where

all irreducible representations can be chosen to be real, and we generalize thereafter. We begin by symmetrizing the variables $\{u_1, \ldots, u_N\}$ according to the irreducible representations of the group, denoted as $\{u_1, \ldots, u_N\}$. The symmetrized force derivatives with respect to the measurement basis can be constructed using the chain rule as

$$\frac{\partial F_j}{\partial \theta_i} = \sum_k \frac{\partial^2 V}{\partial u_j \partial u_k} \frac{\partial u_k}{\partial \theta_i}, \quad j = 1, \ldots, N. \quad (1)$$

At second order, the great orthogonality theorem [13] dictates that there can be coupling only between the same row of the same type of a given irreducible representation. Key quantities of a given irreducible representation α are the dimension and the number of instances, denoted as ℓ_α and a_α, respectively. Therefore, the matrix $V_{ij} = \frac{\partial^2 V}{\partial u_i \partial u_j}$ can be block diagonalized with $a_\alpha \times a_\alpha$ blocks, where each element of the upper diagonal is an irreducible derivative, and each unique block will repeat ℓ_α times. Given that different irreducible representations do not couple, they can always be bundled into a single measurement, and therefore, the only question is how many measurements are needed to extract all repeating irreducible representations. Given n measurements, the chain rule for a given row of the irreducible representation α can be written as

$$\begin{bmatrix} \frac{\partial F_{i_1}}{\partial \theta_1} & \cdots & \frac{\partial F_{i_1}}{\partial \theta_n} \\ \vdots & \ddots & \vdots \\ \frac{\partial F_{i_{a_\alpha}}}{\partial \theta_1} & \cdots & \frac{\partial F_{i_{a_\alpha}}}{\partial \theta_n} \end{bmatrix} = V_\alpha \begin{bmatrix} \frac{\partial u_{i_1}}{\partial \theta_1} & \cdots & \frac{\partial u_{i_1}}{\partial \theta_n} \\ \vdots & \ddots & \vdots \\ \frac{\partial u_{i_{a_\alpha}}}{\partial \theta_1} & \cdots & \frac{\partial u_{i_{a_\alpha}}}{\partial \theta_n} \end{bmatrix}, \quad (2)$$

where V_α is the subblock of V corresponding to the irreducible representation α and $\{i_1, \ldots, i_{a_\alpha}\}$ are labels of the given row of the irreducible representation α. We first consider the case of one-dimensional irreducible representations and then generalize to the multidimensional case. If $n \geq a_\alpha$, then V_α can be solved for via matrix inversion given that the rightmost matrix in Eq. (2) is chosen to be full rank. Therefore, for one-dimensional irreducible representations, we have $N_m = \max_\alpha a_\alpha$. In the general case where there may be repeating multidimensional irreducible representations, each row forms an independent subspace with an identical $a_\alpha \times a_\alpha$ potential, and therefore, one can bundle different rows of different instances of a given irreducible representation, resulting in

$$N_m = \max_\alpha \lceil a_\alpha / \ell_\alpha \rceil. \quad (3)$$

To illustrate an application of Eq. (3), consider a three-atom molecule invariant to C_{3v}, such as H_3^+ [14], where we constrain the atoms to move in plane. The displacement representation decomposes to $2E + A_1 + A_2$, resulting in $N_m = 1$, because the repeating multidimensional E irreducible representations can be bundled into the same measurement. The condition number of the chain rule matrix is naturally minimized by taking equal weights of each row of each irreducible representation present in a given bundle, where repeating rows are bundled separately, yielding a condition number of 1 and hence zero amplification of error. To prove this, consider $\theta_i = (1/|\tilde{s}_i|) \sum_{j \in \tilde{s}_i} u_j$, where $\tilde{s}_i$ is the set of labels of irreducible displacements contained in the measurement θ_i. For $j \in \tilde{s}_i$, the partial derivatives of θ_i are $\frac{\partial \theta_i}{\partial u_j} = 1/|\tilde{s}_i|$, and the pseudoinverse is used to obtain $\frac{\partial u_j}{\partial \theta_i} = 1$. The chain rule matrix is therefore

the identity matrix, and the condition number is the identity. The irreducible derivatives probed by θ_i are then obtain as $\frac{\partial^2 V}{\partial u_k \partial u_j} = \frac{\partial^2 V}{\partial u_k \partial \theta_i}$ for $j \in \tilde{s}_i$.

We consider several simple examples to illustrate the preceding formulation, beginning with the classical coupled oscillator with mirror symmetry, having potential $V = \frac{1}{2}(\gamma_A u_A^2 + \gamma_B u_B^2)$, where u_A and u_B are symmetrized modes that transform like irreducible representations of the order 2 group, and $N_d = 2$. In this case, there is only one instance of each type of irreducible representation, with both being one-dimensional, and therefore, $N_m = 1$. The condition number optimized basis is then obtained by taking equal weights of each irreducible vector, yielding $\theta_1 = (u_A + u_B)/2$. The irreducible derivatives $\boldsymbol{d} = (\gamma_A, \gamma_B)^\mathsf{T}$ can be extracted from the measurements $\boldsymbol{f} = (\frac{\partial F_A}{\partial \theta_1}, \frac{\partial F_B}{\partial \theta_1})^\mathsf{T}$ as $\boldsymbol{d} = \boldsymbol{f}$.

The preceding example does not have repeating irreducible representations, so we now consider the three-atom oscillator with mirror symmetry, where the potential in terms of the symmetrized modes is $V = \frac{1}{2}(\gamma_A u_A^2 + \gamma_B u_B^2 + \gamma_{B'} u_{B'}^2 + \gamma_{BB'} u_B u_{B'})$ and $N_d = 4$. In this case, the one-dimensional B irreducible representation repeats twice, and therefore, $N_m = 2$. The irreducible derivative γ_A can be bundled into the measurement of either $\gamma_B, \gamma_{BB'}$ or $\gamma_{B'}, \gamma_{BB'}$ or both while maintaining a condition number of 1. Therefore, a possible condition number optimized basis is $\theta_1 = (u_A + u_B)/2$ and $\theta_2 = u_{B'}$. The irreducible derivatives $\boldsymbol{d}_1 = (\gamma_A, \gamma_B, \gamma_{BB'})$ are extracted from the measurement derivatives $\boldsymbol{f}_1 = (\frac{\partial F_A}{\partial \theta_1}, \frac{\partial F_B}{\partial \theta_1}, \frac{\partial F_{B'}}{\partial \theta_1})^\mathsf{T}$ as $\boldsymbol{d}_1 = \boldsymbol{f}_1$. The irreducible derivatives $\boldsymbol{d}_2 = (\gamma_{B'}, \gamma_{BB'})$ are extracted from the measurement derivatives $\boldsymbol{f}_2 = (\frac{\partial F_{B'}}{\partial \theta_2}, \frac{\partial F_B}{\partial \theta_2})^\mathsf{T}$ as $\boldsymbol{d}_2 = \boldsymbol{f}_2$.

The preceding formalism and examples all pertain to ambivalent groups, which can always have real irreducible representations. In general, the translation group is not ambivalent and will have complex irreducible representations. However, we will demonstrate that the formulation for ambivalent groups can be applied with trivial modifications. The basic idea is to apply the preceding formalism to the factor group of the q point, denoted $\mathfrak{P}(\boldsymbol{q})$ in the notation of Birman [15], for each q point in the irreducible Brillouin zone. Given that we are focused on hierarchical supercell BID, we need to consider only $\boldsymbol{q}$ and $\bar{\boldsymbol{q}}$ pairs individually [1]. We consider the simplest nontrivial example, which can then be extended to the general case. Consider the one-dimensional chain with two distinct atoms per unit cell and a system size of three unit cells. There will be three q points: Γ, Δ, and $\bar{\Delta}$. The translationally symmetrized potential energy is given as

$$V = \frac{1}{2} d_{\Gamma\Gamma}^{oo} u_\Gamma^o u_\Gamma^o + d_{\Delta\Delta}^{aa} u_\Delta^a u_\Delta^a + d_{\Delta\Delta}^{bb} u_\Delta^b u_\Delta^b \\ + \left(d_{\Delta\Delta}^{ab} u_\Delta^a u_\Delta^b + \text{c.c.} \right), \quad (4)$$

where a and b label different instances of the identity representation of the little group at the Δ point. While $d_{\Gamma\Gamma}^{oo}$, $d_{\Delta\Delta}^{aa}$, and $d_{\Delta\Delta}^{bb}$ are real numbers, $d_{\Delta\Delta}^{ab}$ is complex, and both the real and imaginary parts must be computed. Given that atoms can be displaced only on the real axis, a change of basis is required when performing finite-displacement computations. For q points with complex irreducible representations, a unitary transformation to the real-q representation [1,16] is given

as

$$u_{\boldsymbol{q}^c} = \frac{1}{\sqrt{2}}(u_{\boldsymbol{q}} + u_{\bar{\boldsymbol{q}}}), \qquad u_{\boldsymbol{q}^s} = \frac{i}{\sqrt{2}}(u_{\bar{\boldsymbol{q}}} - u_{\boldsymbol{q}}). \quad (5)$$

The potential can be transformed to the real-q representation as

$$\begin{aligned}
V = {}& \frac{1}{2} d_{\Gamma\Gamma}^{o\,o} u_{\Gamma}^{o} u_{\Gamma}^{o} + \frac{1}{2} d_{\Delta\Delta}^{a\,a} \left(u_{\Delta^c}^{a} u_{\Delta^c}^{a} + u_{\Delta^s}^{a} u_{\Delta^s}^{a} \right) \\
& + \frac{1}{2} d_{\Delta\Delta}^{b\,b} \left(u_{\Delta^c}^{b} u_{\Delta^c}^{b} + u_{\Delta^s}^{b} u_{\Delta^s}^{b} \right) \\
& + \mathrm{Re}\big(d_{\Delta\Delta}^{a\,b}\big) \left(u_{\Delta^c}^{a} u_{\Delta^c}^{b} + u_{\Delta^s}^{a} u_{\Delta^s}^{b} \right) \\
& + \mathrm{Im}\big(d_{\Delta\Delta}^{a\,b}\big) \left(u_{\Delta^s}^{a} u_{\Delta^c}^{b} - u_{\Delta^c}^{a} u_{\Delta^s}^{b} \right). \quad (6)
\end{aligned}$$

Here we see that the real-q representation can be viewed as doubling the dimension of the irreducible representation of the little group, with the caveat that the repeating irreducible representations have different phase conventions and different rows of different instances of an irreducible representation may now couple (e.g., $u_{\Delta^c}^{a}$ couples with $u_{\Delta^s}^{b}$). The fact that $d_{\Delta\Delta}^{a\,b}$ is complex precludes any gain from $u_{\boldsymbol{i}}^{i}$ and $u_{\bar{\boldsymbol{i}}}^{i}$ being complex conjugates, and the same conclusion holds in the case of multidimensional irreducible representations of the little group. Therefore, the number of measurements is obtained by applying Eq. (3) to the irreducible representations obtained from symmetrizing according to $\mathfrak{P}(\Delta)$, and one may bundle either the c or s vector as in the case of the ambivalent group, with the caveat that the minus sign in Eq. (6) must be accounted for. The irreducible derivative associated with the Γ point can be bundled within the Δ point measurements given that Γ is commensurate with all supercells. One choice for the condition number optimized basis is $\theta_1 = (u_{\Gamma}^{o} + u_{\Delta^s}^{a})/2$ and $\theta_2 = u_{\Delta^c}^{b}$. The irreducible derivatives $\boldsymbol{d}_1 = (d_{\Gamma\Gamma}^{o\,o}, d_{\Delta\Delta}^{a\,a}, \mathrm{Re}(d_{\Delta\Delta}^{a\,b}), \mathrm{Im}(d_{\Delta\Delta}^{a\,b}))$ are extracted from the measurement derivatives $\boldsymbol{f}_1 = (\frac{\partial F_{\Gamma}^{o}}{\partial\theta_1}, \frac{\partial F_{\Delta s}^{a}}{\partial\theta_1}, \frac{\partial F_{\Delta s}^{b}}{\partial\theta_1}, \frac{\partial F_{\Delta c}^{b}}{\partial\theta_1})^{\mathsf{T}}$ as $\boldsymbol{d}_1 = \boldsymbol{f}_1$. The irreducible derivatives $\boldsymbol{d}_2 = (d_{\Delta\Delta}^{b\,b}, \mathrm{Re}(d_{\Delta\Delta}^{a\,b}), \mathrm{Im}(d_{\Delta\Delta}^{a\,b}))$ are extracted from the measurement derivatives $\boldsymbol{f}_2 = (\frac{\partial F_{\Delta c}^{b}}{\partial\theta_2}, \frac{\partial F_{\Delta c}^{a}}{\partial\theta_2}, \frac{\partial F_{\Delta s}^{a}}{\partial\theta_2})^{\mathsf{T}}$ as $\boldsymbol{d}_2 = \boldsymbol{f}_2$. A general crystal will have more q points and more irreducible representations at each q point, but given that each q point corresponds to a different irreducible representation of the translation group, each $\boldsymbol{q}/\bar{\boldsymbol{q}}$ pair can be treated separately, and thus, each piece of the problem maps onto the preceding example.

In the preceding case, both the real and imaginary parts of the cross derivatives between irreducible representations must be measured. An appropriate gauge transformation can make the cross derivative purely real, but this transformation cannot be known *a priori* in general. However, if the space group has a point symmetry operation that maps $\boldsymbol{q} \leftrightarrow \bar{\boldsymbol{q}}$, the proper phase convention can be determined *a priori*, and then all irreducible derivatives will be real. In this case, the real-q basis can be viewed as doubling the dimension of the irreducible representation of the little group without any caveat, and thus, the number of measurements is $N_m = \max_{\alpha}\lceil a_{\alpha}/(2\ell_{\alpha})\rceil$. To illustrate this reduction, consider the potential from Eq. (6) but make the atoms equivalent, which results in a mirror plane that maps $\Delta \leftrightarrow \bar{\Delta}$. Therefore, a phase convention can be chosen *a priori* such that $\mathrm{Im}(d_{\Delta\Delta}^{a\,b}) = 0$ and

$N_m = 1$. A condition number optimized basis can be chosen as $\theta_1 = (u_{\Gamma}^{o} + u_{\Delta^c}^{a} + u_{\Delta^s}^{b})/3$. The irreducible derivatives $\boldsymbol{d}_1 = (d_{\Gamma\Gamma}^{o\,o}, d_{\Delta\Delta}^{a\,a}, d_{\Delta\Delta}^{a\,a}, d_{\Delta\Delta}^{b\,b})$ are extracted from the measurement derivatives $\boldsymbol{f}_1 = (\frac{\partial F_{\Gamma}^{o}}{\partial\theta_1}, \frac{\partial F_{\Delta c}^{a}}{\partial\theta_1}, \frac{\partial F_{\Delta c}^{b}}{\partial\theta_1}, \frac{\partial F_{\Delta s}^{b}}{\partial\theta_1})^{\mathsf{T}}$ as $\boldsymbol{d}_1 = \boldsymbol{f}_1$.

In the preceding we have outlined a condition number optimized measurement basis, and now we present guidelines for resolving a sensitivity associated with a given phonon mode. In our CNO basis, each irreducible derivative can be traced to a specific bundle, and the simplest solution will be to reevaluate the choice of Δ and or increase the convergence parameters for that particular bundle. However, given that energy derivatives normally converge faster than force derivatives, one could also recompute the problematic irreducible derivatives using LID_0 and use them in place of the erroneous BID result, which we refer to as a hybrid LID-BID approach.

III. RESULTS

We now illustrate LID, BID, and hybrid LID-BID in several crystals where there are discrepancies from the existing literature, including AuZn and bcc Li. DFT calculations were performed using the projector augmented wave (PAW) method [17,18], as implemented in the Vienna Ab initio Simulation Package (VASP) [19–22]. The Perdew-Burke-Ernzerhof generalized gradient approximation (GGA) [23] was used for results in the main text, and local density approximation (LDA) [24] results for AuZn are provided in the Supplemental Material [25]. Unless otherwise noted, a plane wave basis with a kinetic energy cutoff of 1200 and 450 eV was employed for Li and AuZn, respectively. A Γ-centered k-point mesh of $30 \times 30 \times 30$ was used in calculations of the primitive unit cell in both AuZn and Li, and corresponding k-point densities were used in supercells. The k-point integrations were done using the tetrahedron method with Blöchl corrections [26]. The DFT energies were converged to within 10^{-6} eV, while ionic relaxations were converged to within 10^{-5} eV. For AuZn, we used the experimental lattice parameter $a_0 = 3.13$ Å in order to make a comparison with previous calculations, while energy minimization yielded a lattice parameter of 2.97 Å for Li, and the relaxed trigonal structure of AuZn is provided in the Supplemental Material [25]. For the central finite-difference calculations within LID and BID, quadratic error tails were constructed using the best three out of at least eight discretizations (i.e., Δ in Eq. (40) in Ref. [1]). It should be noted that many phonon finite-difference calculations are performed with forward finite difference and a single discretization, and LID and BID can be executed in this manner, although this choice would not extrapolate the discretization error to zero. Elastic constants were measured using ϵ-LID_0, which uses second strain derivatives of the energy. For LID and BID in Li and cubic AuZn, the Brillouin zone is discretized using real-space supercells of $8 \times 8 \times 8$ (i.e., multiplicity 512 and 512 atoms) and $6 \times 6 \times 6$ (i.e., multiplicity 216 and 432 atoms), respectively, which are encoded as $\hat{\boldsymbol{S}}_{\mathrm{BZ}} = 8\hat{\boldsymbol{1}}$ and $\hat{\boldsymbol{S}}_{\mathrm{BZ}} = 6\hat{\boldsymbol{1}}$. While LID and BID construct all irreducible derivatives commensurate with $\hat{\boldsymbol{S}}_{\mathrm{BZ}} = 8\hat{\boldsymbol{1}}$ and $\hat{\boldsymbol{S}}_{\mathrm{BZ}} = 6\hat{\boldsymbol{1}}$ in Li and cubic AuZn, respectively, all results are extracted from supercells with multiplicity 8 and 6 [1,27]. For LID and BID in trigonal AuZn, the Brillouin zone is dis-
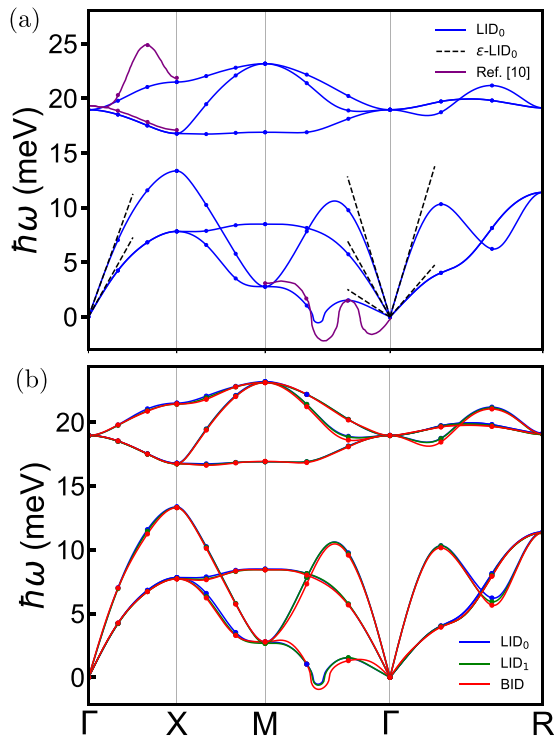
FIG. 1. DFT phonon dispersion of cubic AuZn, where points are computed values and lines are a Fourier interpolation. (a) LID_0 results are shown in blue, the acoustic dispersion obtained from the elastic constants is shown as black dashed lines, and the results shown in purple are taken from Ref. [10]. (b) LID_0, LID_1, and BID results are shown in blue, green, and red, respectively.

cretized using $\hat{\mathbf{S}}_{BZ} = 2\hat{\mathbf{1}}$ (i.e., multiplicity 8 and 144 atoms), and all irreducible derivatives are extracted using supercells with multiplicity 2. For phonon band structure plots, a table of q-point labels is provided [25].

We begin by analyzing the cubic phase of AuZn, where experiment dictates that there is a phase transition to the trigonal structure, which is connected to the cubic structure via a distortion along q vectors in the star of $\boldsymbol{q} = (\frac{1}{3}, \frac{1}{3}, 0)$. Inelastic x-ray scattering experiments at $T = 200\,\mathrm{K}$ indicate that there is a nearly soft phonon mode at $\boldsymbol{q} = (\frac{1}{3}, \frac{1}{3}, 0)$ [9], which can be identified as a B_2 mode under the C_{2v} little group. There are two B_2 basis modes at $\boldsymbol{q} = (\frac{1}{3}, \frac{1}{3}, 0)$, and each one can be purely constructed of either Au or Zn, while the eigenmodes will be a linear combination. In order to study the B_2 eigenmodes, one must compute the second derivative of each basis mode and the coupling between the two, resulting in three real irreducible derivatives given that AuZn has inversion symmetry. Therefore, when precisely computing the B_2 eigenmodes, three error tails must be carefully scrutinized.

We proceed by presenting the phonons of the cubic phase of AuZn computed using LID_0 [see Fig. 1(a)]. Blue points represent direct measurements of the phonons via LID_0, solid blue lines are Fourier interpolations, and dashed black lines are the linear dispersion of the acoustic modes obtained independently from the elastic constants computed using $\epsilon\text{-}LID_0$ (see [25] for error tails). Previously published results [10] using finite displacement are shown as purple lines for branches

with major discrepancies. Both sets of results contain all derivatives within the same finite translation group defined by a $\hat{\mathbf{S}}_{BZ} = 6\hat{\mathbf{1}}$ supercell, and therefore, values from Ref. [10] are measured at the same discrete points as our calculations. Along the plotted directions, the finite-displacement measurements from Ref. [10] are in reasonable agreement with our own results, with the major exception of a single spurious point on the highest optical branch between Γ and X, highlighting the importance of constructing error tails. The resulting Fourier interpolation in Ref. [10] yields imaginary frequencies for the acoustic branches near the Γ point, indicating that some elastic constant is negative. However, our results clearly prove that the elastic constants are positive, and therefore, the Fourier interpolation of the finite-displacement results from Ref. [10] are likely contaminated by the spurious measurement. The DFPT results from Ref. [10] differ substantially from our results for the lower B_2 branch between Γ and M, and the $\boldsymbol{q} = (\frac{1}{3}, \frac{1}{3}, 0)$ point is predicted to be soft. The DFPT and finite-displacement results must agree when both are converged. It should be noted that a different pseudopotential was used in the DFPT calculation, which could be the source of some differences. Additionally, the DFPT results used a smearing k-space integration technique, and it is not clear whether the results are converged with respect to the k-point density. Our own DFPT calculations [28,29] using the tetrahedron method indicate that the mode is not soft, and the phonon energy is in reasonable agreement with our LID_0 results (see Fig. S2 [25]). While the GGA results using the VASP PAWs and the experimental lattice parameter do not yield a soft mode, using LDA under these conditions will yield a soft mode [25]. Additionally, using GGA with the relaxed lattice parameter will also yield a soft mode. Therefore, the physics of the B_2 mode is somewhat sensitive and requires a detailed investigation to provide a robust comparison with experiment.

Having established the precise phonon spectrum using LID_0, we now proceed to assess the precision of BID using the CNO basis and LID_1 [see Fig. 1(b)]. Given the importance of the B_2 modes at $\boldsymbol{q} = (\frac{1}{3}, \frac{1}{3}, 0)$, we will retain the LID_0 result for the two-dimensional B_2 block, and all other results will be obtained from BID and LID_1, respectively. We see that LID_1 and BID introduce only small errors, although the magnitudes of the errors are always larger in BID, as expected. Having demonstrated the fidelity of BID, we use BID to compute the phonons in the trigonal phase using C_1 symmetry (see Fig. 2). The only previous result in the literature that we are aware of is a phonon DOS [30], but that study used a crystal structure which was not fully relaxed.

We now consider the phonons of Li metal in the bcc phase, and we begin by focusing on the lowest-frequency branch between Γ and N [see Fig. 3(a)], as unusual results were obtained in previously published DFT calculations [12]. It is worth noting that this anomaly is not observed in inelastic neutron scattering measurements at $T = 98\,\mathrm{K}$ [11]. We follow our protocol of investigating with LID_0, ensuring proper error tails are obtained and testing convergence with respect to electronic k-point density. In Fig. 3(a), circles represent direct measurements of the phonons via LID_0 at various k-point mesh densities for $\hat{\mathbf{S}}_{BZ} = 8\hat{\mathbf{1}}$ and $\hat{\mathbf{S}}_{BZ} = 10\hat{\mathbf{1}}$, the blue line is a Fourier interpolation of $\hat{\mathbf{S}}_{BZ} = 8\hat{\mathbf{1}}$ using an electronic k-point
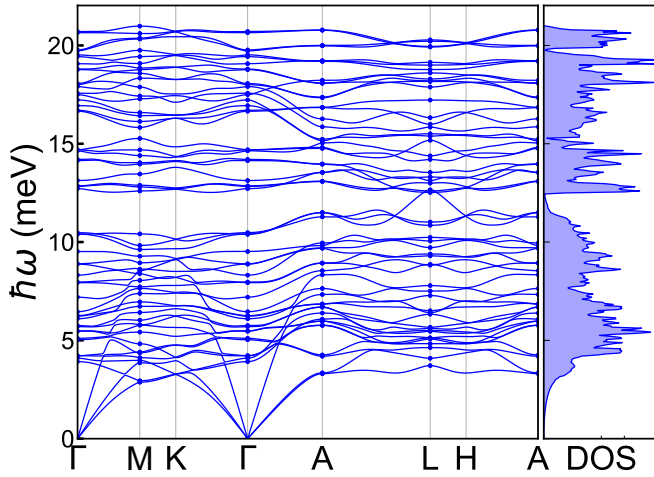
FIG. 2. DFT phonon dispersion and DOS of trigonal AuZn computed using BID.

FIG. 3. (a) DFT phonons of Li for the lowest branch along Γ-N computed using LID_0, where points are computed values and lines are a Fourier interpolation using $\hat{\mathbf{S}}_{\text{BZ}} = 8\hat{\mathbf{1}}$. LID results are provided for electronic k-point meshes of $20\hat{\mathbf{1}}$ and $40\hat{\mathbf{1}}$, and results from Ref. [12] are shown in green. (b)–(e) Select discrete second energy derivatives for the lowest branch vs displacement magnitude, where δ is the real-space amplitude, which is modulated throughout the supercell as $\delta \cos(2\pi \boldsymbol{q} \cdot \boldsymbol{t})$. Each line is a fit to a quadratic for the three points which yield the smallest error, and the intercept yields the irreducible derivative of the respective mode. LID_1 results are included in (b).

mesh of $40\hat{\mathbf{1}}$, and the dashed black line is the linear dispersion of the acoustic mode obtained from the ϵ-LID_0 elastic constants (see [25] for additional k-point densities). The results of Ref. [12] using finite-displacement calculations with $\hat{\mathbf{S}}_{\text{BZ}} = 10\hat{\mathbf{1}}$ are shown as green diamonds and lines for the measured and interpolated results, respectively. The results of Ref. [12] are in reasonable agreement with our $20\hat{\mathbf{1}}$ k-point mesh results with the exception of $\boldsymbol{q} = (\frac{1}{5}, 0, 0)$. The most obvious difference between our LID_0 calculations and those of Ref. [12] is that our result uses second energy derivatives and quadratic error tails, while the latter uses first force derivatives and a single Δ. Both of these differences are likely to contribute to the $\boldsymbol{q} = (\frac{1}{5}, 0, 0)$ discrepancy of Ref. [12]. It is important to explore the error tails of the discretized second energy derivatives (Eq. (40) in Ref. [1]) in order to understand the potential issues of using a single Δ [Figs. 3(b)–3(e)]. For a given Δ, the amplitude of the real-space displacements modulates as $\delta \cos(2\pi \boldsymbol{q} \cdot \boldsymbol{t})$ throughout the supercell [1], and the resulting discretized second energy derivatives are plotted as a function of δ. For the case of $\boldsymbol{q} = (\frac{1}{2}, 0, 0)$ [Fig. 3(b)], the k mesh of $20\hat{\mathbf{1}}$ strongly deviates from a quadratic below $\delta = 0.1$ Å, indicating that fitting larger δ to a quadratic error tail is critical to obtaining reasonable results at this k-point density. However, increasing to $40\hat{\mathbf{1}}$ yields a clear quadratic behavior down to $\delta = 0.02$ Å. It is also instructive to evaluate the corresponding LID_1 force derivative for $40\hat{\mathbf{1}}$, which does not show signs of quadratic behavior until large δ, demonstrating the limitation of force derivatives. This case illustrates how using a single Δ could yield nontrivial errors. For $\boldsymbol{q} = (\frac{3}{8}, 0, 0)$ [see Fig. 3(c)], $20\hat{\mathbf{1}}$ has only three points falling onto a quadratic curve, while $40\hat{\mathbf{1}}$ has four consecutive points which are strongly quadratic. The quadratic behaviors in $\boldsymbol{q} = (\frac{1}{8}, 0, 0)$ and $\boldsymbol{q} = (\frac{1}{5}, 0, 0)$ for $20\hat{\mathbf{1}}$ and $40\hat{\mathbf{1}}$ are comparable, although the overall change in the intercepts is modest [see Figs. 3(d) and 3(e)]. Therefore, the large difference observed in Ref. [12] is likely connected to a discretization error associated with finite displacements. Additionally, we have demonstrated that there is some sensitivity associated with the electronic k-point mesh density for the lowest branch along Γ-N. It is worth noting that previous

DFPT calculations did not suggest any sensitivity for the aforementioned branch [31] (also see Ref. [32]), although our own results using DFPT [28,29] demonstrate that there is a sensitivity (see Fig. S7 [25]).

We now proceed to compute the entire phonon spectrum using LID_0 [see Fig. 4(a)]. Given the sensitivity observed in Fig. 3, we retain the highest-precision $40\hat{\mathbf{1}}$ k-point mesh results for the irreducible derivatives in this branch, and we use $30\hat{\mathbf{1}}$ otherwise. We see that the results are in good agreement with the linear acoustic dispersions from the elastic constants at small $\boldsymbol{q}$. Having established the LID_0 results, we now proceed to assess the precision of LID_1 and BID using the CNO basis [see Fig. 4(b)]. Once again, we retain the
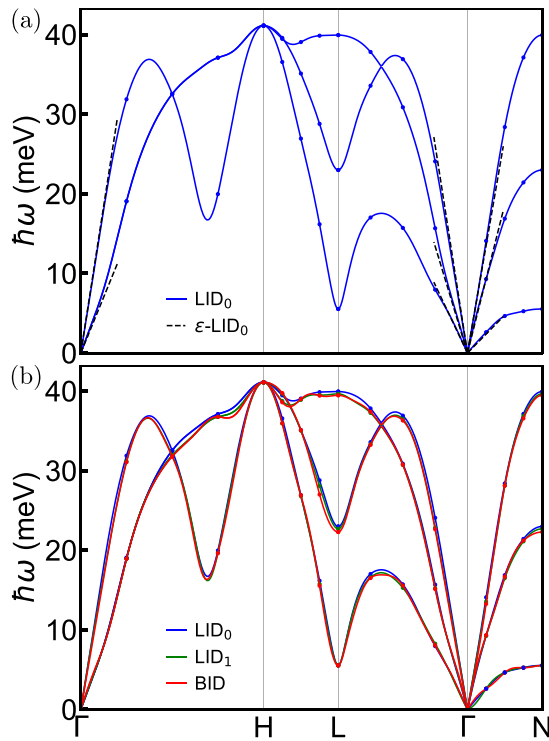
FIG. 4. DFT phonon dispersion of bcc Li, where points are computed values and lines are a Fourier interpolation. (a) LID_0 results are shown in blue, and the acoustic dispersion obtained from the elastic constants is shown by black lines. (b) LID_0, LID_1, and BID results are shown in blue, green, and red, respectively.

highest-precision $40\hat{1}$ LID_0 results for the irreducible derivatives in the branch studied in Fig. 3. We begin by exploring LID_1 to isolate the effect of using first derivatives of the forces in place of second derivatives of the energy. We see that LID_1 introduces only small changes, such as near the H point. These differences are small enough for our purposes, but they could be reduced further by increasing the various convergence parameters of the calculation. In the BID result, where the effect of bundling can be seen by comparing the red curve with the green curve, we can see that the magnitude of the changes is on the same scale as the effect of using forces. Here we see that the large reduction in computational cost is achieved without any appreciable loss in fidelity.

IV. CONCLUSION

In summary, we have shown how to accurately and efficiently compute phonons from first principles using the LID and BID approaches. In previous work, we defined the notion of a condition number optimized bundled basis but did not provide a method to find an optimal solution [1]. Here we derived an optimal solution at second order, enabling BID to provide irreducible derivatives in the smallest number of computations with zero amplification of error. Typically, one will use BID to compute all irreducible derivatives. If there are known sensitivities or if BID error tails are deficient, LID_0 (i.e., using energy derivatives) can be used to compute the problematic irreducible derivatives, replacing the BID result. This hybrid LID-BID approach balances accuracy and efficiency as needed, which is particularly important when computing phonons using beyond DFT methods such as hybrid functionals [33,34], variational quantum Monte Carlo [35,36], and DFT plus dynamical mean-field theory [37].

We demonstrated the fidelity of our irreducible approaches by addressing sensitive phonons from the literature. In the cubic phase of AuZn, we computed the phonons, demonstrated consistency with the computed elastic constants, and resolved discrepancies in previously published calculations. We also computed the phonons in the trigonal phase of AuZn. In elemental Li, we computed the phonons and found that the lowest phonon branch between Γ and N is somewhat sensitive to the electronic k-point mesh density. Additionally, we demonstrated the important role of properly extrapolating the finite-displacement discretization error to zero. While we studied metallic systems in this paper, LO-TO splitting in polar insulators can be treated via the standard dipole-dipole approach [38,39] in conjunction with finite-displacement approaches (see Appendix A in Ref. [6] for a discussion and applications), and therefore, our irreducible derivative approaches can be applied universally. Moreover, a recent extension of the dipole-dipole approach which includes higher-order multipoles [40] can also be employed using finite-displacement approaches.

[1] L. Fu, M. Kornbluth, Z. Cheng, and C. A. Marianetti, Group theoretical approach to computing phonons and their interactions, Phys. Rev. B **100**, 014303 (2019).

[2] K. Parlinski, Z. Q. Li, and Y. Kawazoe, First-Principles Determination of the Soft Mode in Cubic ZrO_2, Phys. Rev. Lett. **78**, 4063 (1997).

[3] D. Alfe, Phon: A program to calculate phonons using the small displacement method, Comput. Phys. Commun. **180**, 2622 (2009).

[4] A. Togo and I. Tanaka, First principles phonon calculations in materials science, Scr. Mater. **108**, 1 (2015).

[5] M. Kawamura, Y. Gohda, and S. Tsuneyuki, Improved tetrahedron method for the Brillouin-zone integration applicable to response functions, Phys. Rev. B **89**, 094515 (2014).

[6] M. A. Mathis, A. Khanolkar, L. Fu, M. S. Bryan, C. A. Dennett, K. Rickert, J. M. Mann, B. Winn, D. L. Abernathy, M. E. Manley, D. H. Hurley, and C. A. Marianetti, Generalized quasiharmonic approximation via space group irreducible derivatives, Phys. Rev. B **106**, 014314 (2022).

[7] M. D. Jong, W. Chen, T. Angsten, A. Jain, R. Notestine, A. Gamst, M. Sluiter, C. K. Ande, S. van der Zwaag, J. J. Plata, C. Toher, S. Curtarolo, G. Ceder, K. A. Persson, and M. Asta,

Charting the complete elastic properties of inorganic crystalline compounds, Sci. Data **2**, 150009 (2015).

[8] T. Makita, A. Nagasawa, Y. Morii, N. Minakawa, and H. Ohno, Phonon-dispersion relations of premartensitic beta(1)-phase in AuZn alloys, Phys. B (Amsterdam, Neth.) **213–214**, 430 (1995).

[9] J. C. Lashley, S. M. Shapiro, B. L. Winn, C. P. Opeil, M. E. Manley, A. Alatas, W. Ratcliff, T. Park, R. A. Fisher, B. Mihaila, P. Riseborough, E. K. H. Salje, and J. L. Smith, Observation of a Continuous Phase Transition in a Shape-Memory Alloy, Phys. Rev. Lett. **101**, 135703 (2008).

[10] L. Isaeva, P. Souvatzis, O. Eriksson, and J. C. Lashley, Lattice dynamics of cubic AuZn from first principles, Phys. Rev. B **89**, 104101 (2014).

[11] H. G. Smith, G. Dolling, R. M. Nicklow, P. R. Vijayaraghavan, and M. K. Wilkinson in *Proceedings of the Conference on Inelastic Neutron Scattering* (International Atomic Energy Agency, Vienna, 1968), p. 149.

[12] M. Hutcheon and R. Needs, Structural and vibrational properties of lithium under ambient conditions within density functional theory, Phys. Rev. B **99**, 014111 (2019).

[13] M. Tinkham, *Group Theory and Quantum Mechanics* (Dover, Mineola, N.Y., 1964).

[14] W. Meyer, P. Botschwina, and P. Burton, *Ab initio* calculation of near-equilibrium potential and multipole moment surfaces and vibrational frequencies of H_3^+ and its isotopomers, J. Chem. Phys. **84**, 891 (1986).

[15] J. L. Birman, Full-group and subgroup methods in crystal physics, Phys. Rev. **150**, 771 (1966).

[16] J. F. Cornwell, *Group Theory in Physics* (Academic, London, 1984), Vol. 1.

[17] P. E. Blochl, Projector augmented-wave method, Phys. Rev. B **50**, 17953 (1994).

[18] G. Kresse and D. Joubert, From ultrasoft pseudopotentials to the projector augmented-wave method, Phys. Rev. B **59**, 1758 (1999).

[19] G. Kresse and J. Hafner, *Ab initio* molecular-dynamics for liquid-metals, Phys. Rev. B **47**, 558 (1993).

[20] G. Kresse and J. Hafner, *Ab initio* molecular-dynamics simulation of the liquid-metal amorphous-semiconductor transition in germanium, Phys. Rev. B **49**, 14251 (1994).

[21] G. Kresse and J. Furthmuller, Efficiency of ab-initio total energy calculations for metals and semiconductors using a plane-wave basis set, Comput. Mater. Sci. **6**, 15 (1996).

[22] G. Kresse and J. Furthmuller, Efficient iterative schemes for *ab initio* total-energy calculations using a plane-wave basis set, Phys. Rev. B **54**, 11169 (1996).

[23] J. P. Perdew, K. Burke, and M. Ernzerhof, Generalized Gradient Approximation Made Simple, Phys. Rev. Lett. **77**, 3865 (1996).

[24] J. P. Perdew and A. Zunger, Self-interaction correction to density-functional approximations for many-electron systems, Phys. Rev. B **23**, 5048 (1981).

[25] See Supplemental Material at http://link.aps.org/supplemental/10.1103/PhysRevB.107.174302 for q-point labels, the AuZn trigonal structure, error tails, the plane wave cutoff and k-point convergence, and select LDA results.

[26] P. E. Blochl, O. Jepsen, and O. K. Andersen, Improved tetrahedron method for Brillouin-zone integrations, Phys. Rev. B **49**, 16223 (1994).

[27] J. H. Lloyd-williams and B. Monserrat, Lattice dynamics and electron-phonon coupling calculations using nondiagonal supercells, Phys. Rev. B **92**, 184301 (2015).

[28] P. Giannozzi *et al.*, QUANTUM ESPRESSO: A modular and open-source software project for quantum simulations of materials, J. Phys.: Condens. Matter **21**, 395502 (2009).

[29] P. Giannozzi *et al.*, Advanced capabilities for materials modelling with Quantum ESPRESSO, J. Phys.: Condens. Matter **29**, 465901 (2017).

[30] M. Sanati, R. C. Albers, T. Lookman, and A. Saxena, First-order versus second-order phase transformation in AuZn, Phys. Rev. B **88**, 024110 (2013).

[31] T. Bazhirov, J. Noffsinger, and M. L. Cohen, Electron-phonon coupling in bcc lithium, Phys. Rev. B **84**, 125122 (2011).

[32] J. P. Perdew and S. H. Vosko, Phonon frequencies of lithium from a local effective potential, J. Phys. F **6**, 1421 (1976).

[33] K. Hummer, J. Harl, and G. Kresse, Heyd-Scuseria-Ernzerhof hybrid functional for calculating the lattice dynamics of semiconductors, Phys. Rev. B **80**, 115205 (2009).

[34] Y. Wang, L. A. Zhang, S. Shang, Z.-K. Liu, and L.-Q. Chen, Accurate calculations of phonon dispersion in CaF_2 and CeO_2, Phys. Rev. B **88**, 024304 (2013).

[35] K. Nakano, T. Morresi, M. Casula, R. Maezono, and S. Sorella, Atomic forces by quantum Monte Carlo: Application to phonon dispersion calculations, Phys. Rev. B **103**, L121110 (2021).

[36] K. K. Ly and D. M. Ceperley, Phonons of metallic hydrogen with quantum Monte Carlo, J. Chem. Phys. **156**, 044108 (2022).

[37] C. P. Koçer, K. Haule, G. L. Pascut, and B. Monserrat, Efficient lattice dynamics calculations for correlated materials with DFT+DMFT, Phys. Rev. B **102**, 245104 (2020).

[38] X. Gonze and C. Lee, Dynamical matrices, Born effective charges, dielectric permittivity tensors, and interatomic force constants from density-functional perturbation theory, Phys. Rev. B **55**, 10355 (1997).

[39] P. Giannozzi, S. de Gironcoli, P. Pavone, and S. Baroni, *Ab initio* calculation of phonon dispersions in semiconductors, Phys. Rev. B **43**, 7231 (1991).

[40] M. Royo, K. R. Hahn, and M. Stengel, Using High Multipolar Orders to Reconstruct the Sound Velocity in Piezoelectrics from Lattice Dynamics, Phys. Rev. Lett. **125**, 217602 (2020).